Soft Matter

PAPER

View Article Online
View Journal | View Issue



Cite this: *Soft Matter*, 2025, **21**, 1233

# Boundaries and cross-linking densities modulate domain sizes of polydomain nematic elastomers†

Takuya Ohzono, [a] Kaoru Katoh [b] and Nariya Uchida [c]

When nematic liquid crystal elastomers (LCEs) crosslinked at their isotropic phase are quenched to the nematic phase, they show polydomain patterns, in which nematic microdomains with different orientations self-organize into a three-dimensional mosaic with characteristic correlation patterns. The orientational correlation length of the domain, which is usually in the micrometer range, is believed to emerge as a result of a competition between liquid crystalline ordering and frozen network inhomogeneity. Although polydomain patterns show potentials as the basic platform for optical, memory, and mechanical devices, no study exists regarding how they are modulated by experimentally accessible parameters. Here, using confocal polarized fluorescence microscopy, we study the effects of a solid-wall or open boundary on the domain size in conjunction with effects of cross-linking density. The LCE bounded by solid glass shows reduced domain size near the boundary. In contrast, increased domain size appears at the free surface. With increasing cross-linking density, the domain size decreases, also exhibiting the boundary effects. Guided by theoretical considerations, the results are explained by a picture that the effective strength of the inhomogeneity frozen in the polymer network, *i.e.*, the effective disorder strength, varies depending on the cross-linking density and constrained states at boundaries. The results offer the first experimental approach to global and local modulation of the polydomain pattern in nematic LCEs.

Received 29th November 2024,
Accepted 10th January 2025

DOI: 10.1039/d4sm01419g

rsc.li/soft-matter-journal



## Introduction

The orientational order of molecular units within soft matter can often be of critical importance to its properties. Low-molecular weight liquid-crystals (LCs)[1] and LC polymeric engineering plastics[2] are well known examples where the molecular orientational order determines their optical and mechanical properties. To manage the functions the control of the molecular order over the material is fundamental. For non-cross-linked LC materials, the alignment can be actively imposed by electric, magnetic, or mechanical stimuli. As the less active method, boundary effects are often employed, in which the molecular units close to the boundary are constrained by the interfacial anchoring effects, including the molecular interaction and anisotropic-topography-induced alignment.[3,4] The alignment at the interface/boundary is transferred to the bulk by the long-ranged LC order.

In the case of weakly cross-linked LC polymers, *i.e.*, LC elastomers (LCEs),[5] focused on in the present study, the polymer network imposes relatively strong translational and rotational constraints to the molecular units. As a result, the alignment method in LCEs after cross-linking is limited to the mechanical one, such as stretching[6] and shearing, in which the externally applied load is directly transmitted through the polymer network. While the cross-links cause this technical limitation in controlling alignment, it leads to the crucial coupling between the alignment and the macroscopic polymer network, which is absent in the low-molecular weight LCs and LCPs. Owing to the nature, the LCEs cross-linked under the uniaxially aligned state, which is often called monodomain LCEs, show drastic deformation[6] upon the phase transition between the nematic and isotropic states, leading to the soft-actuator studies as predicted by de Gennes.[7]

Meanwhile, LCEs cross-linked at the isotropic state, *i.e.*, without alignment, are known to show, upon entering the nematic phase, a characteristic nematic domain pattern without macroscopic deformation. This is called the polydomain and shows a mosaic of small randomly oriented nematic domains.[5,8] The polydomain is a self-organized pattern of birefringent nematic domains with the typical correlation on the micrometre length scale. If the correlation length and/or periodicity of the polydomain can be controlled, this system may be applied as an optical material with a designed light scattering, and modulation of its mechanical properties, such as stress generation and actuation,[9,10] originating from the

[a] *Research Institute for Electronics and Photonics, National Institute of Advanced Industrial Science and Technology (AIST), 1-1-1 Higashi, Tsukuba 305-8565, Japan. E-mail: ohzono-takuya@aist.go.jp*
[b] *Biomedical Research Institute, AIST, 1-1-1 Higashi, Tsukuba 305-8566, Japan*
[c] *Department of Physics, Tohoku University, Sendai 980-8578, Japan*

† Electronic supplementary information (ESI) available. See DOI: https://doi.org/10.1039/d4sm01419g

anisotropic and soft deformation[11,12] ability of nematic domains also may be expected. As a related periodic structure to the polydomain, a self-organized stripe domain with a similar periodic length scale is known to form after shrinkage of the monodomain in the alignment direction[5,13–21] and the stabilized versions indeed work as anisotropic light diffusers with dynamic tunability.[22,23] Thus, the polydomain textures form a potentially critical morphology for the optical and mechanical effects in LCEs.

However, to date, no experimental study has been conducted that investigates the control of polydomain structures, particularly in terms of their correlation length within the bulk, and how these structures are influenced by the presence of interacting boundaries. In some pioneering theoretical studies,[24,25] it is expected that the length may result from the competition between the nematic ordering and the disordering effects of local random sources on the cross-linked polymer network. Unfortunately, there is no result experimentally supporting the theoretical prediction even qualitatively. The effect of the boundary is far more unknown and is an open question that is also relevant to a wide range of cross-linked polymeric systems, being cured often in contact with the mold surface. Therefore, the focus of this study is to assess the extent to which the polydomain structures of main-chain LCEs at interfaces and the bulk are controlled through the effects of the boundaries and cross-linking density.

As the cross-linked polymer networks are terminated at the boundaries, the constraint imposed by them including the nematic anchoring effect differs from the bulk state. These network states may modulate the polydomain structure at experimentally observable levels. In the case of the LCE interface between glass and air, the constraint should be stronger or weaker than that of the bulk, respectively. As cross-linking density is related to the frozen disorder strength of the network introduced in the previous theoretical discussion,[24–26] the observed modulation on the polydomain pattern would help in evaluating the validity of the theoretical model.

In this study, the effects of experimentally accessible two conditions, boundaries and cross-linking density, on the polydomain patterns are uncovered *via* scanning confocal polarized fluorescence microscopy (cPFOM). With the help of the previously developed theoretical model,[25] the physical backgrounds of the polydomain formation and the results are discussed.

cPFOM is a reflection-mode method, in which the polarized fluorescence light induced by the focused excitation laser light is collected from the same side of the sample. LCEs are homogeneously doped with a dichroic dye that aligns with the local nematic orientation.[22,27–30] The emitted polarized fluorescence directly maps the local nematic director component projected on the polariser axis with a higher spatial resolution than that of conventional polarized optical microscopy. The resolution in the thickness direction is also possible owing to the confocal mode. Thus, although the resolution becomes worse as the scanning point goes into the sample due to the loss of light intensity, nematic orientation patterns are imaged to a depth of approximately a micrometre from the surface. If the sample is properly freeze-cracked,[22] the polydomain textures formed at the bulk are also imaged. Thus, the cPFOM is probably the best tool currently available for characterizing real-space polydomain patterns at both interfaces and the bulk.

It is emphasized that the conventional methods, such as electron, X-ray or neutron techniques, to characterize the different chemistries or submicron electron/atomic density distributions in the polymers, for example, the micro-phase-separated systems, cannot be applied to the observation of the present polydomain. Since different domains in the polydomain textures have identical chemistries, selectively dying them is considerably challenging. Although the depolarized light scattering (DPLS) method has also been used to corroborate the polydomain patterns,[29,31,32] the obtained reverse-space anisotropic scattering patterns including the average information over the sample thickness without local information.

## Results and discussion

### LCE samples and observation modes

Three room-temperature main-chain LCEs with different cross-linker amounts were prepared using the same monomers (see Experimental, Fig. 1a and b). Nominal crosslinking densities, $n_{XD}$, increase as 0.029, 0.043, and 0.141 nm$^{-3}$ in the order X2, X3, and X10 (Fig. 1b) by assuming the LCE density to be on the order of 1 g cm$^{-3}$. The samples in the isotropic phase at the elevated temperature (90 °C) covered with the glass

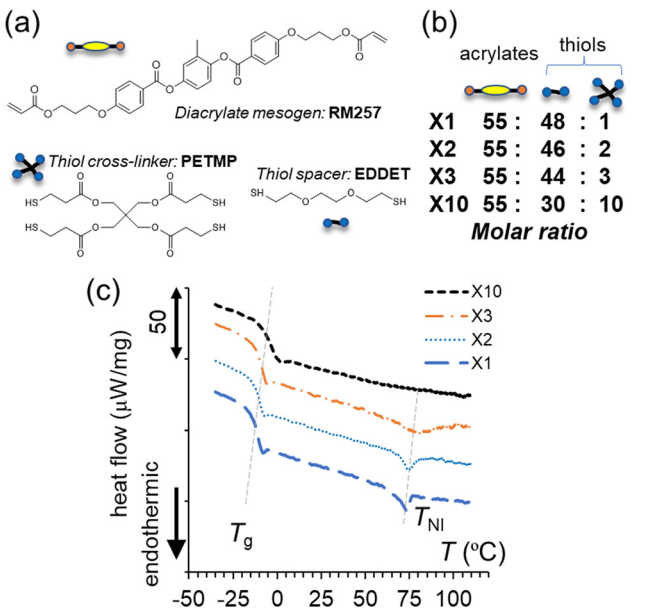


Fig. 1 Main-chain LCEs. (a) Monomers. (b) Molar ratios with different cross-linker amounts. X2, X3, and X10 are mainly characterized. (c) The DSC thermograms on heating at the rate of 5 °C min$^{-1}$. Although the X10 sample shows an unclear $T_{NI}$ peak, the visual observation upon heating suggested that the clearing point was approximately 75 °C. As a reference, X1, which is in the sol state, *i.e.*, a flowable liquid crystal polymer, is also shown.

surface or uncovered were quenched to the room temperature to induce the isotropic–nematic phase transition, upon which the polydomain pattern developed. The formed polydomain states were then fixed by the photo-induced secondary cross-linking between excess acrylates to stabilize the self-organized patterns against the following optical observation and the freeze-cracking process for bulk characterization. When the cross-linker amount was less than that of X2, the sample, X1, became flowable, corresponding to the sol state without the self-supporting ability. The sol sample showed a typical schlieren texture with topological defects[27,33,34] as in the low molecular nematic LCs instead of the polydomain (Fig. S1, ESI†).

The thermal analysis of the LCEs after first crosslinking using differential scanning calorimetry (DSC) (Fig. 1c) showed their nematic–isotropic transition temperatures ($T_{NI}$) around 75 °C and their slight increase with $n_{XD}$. The glass transition temperature ($T_g$) followed a similar trend. The unsharpened transition peaks with $n_{XD}$ suggests that the phase transition was diffused with $n_{XD}$. The strength (or density) of the frozen random disorder in the network, which generally disturbs nematic ordering, should have a positive correlation with density of the cross-links.[24–26] Thus, our LCEs may be viewed as having different disorder strengths, under which the domain size has been theoretically expected to be modulated. Our LCEs typically showed soft elasticity under uniaxial tensile strain of approximately 0.9 (Fig. S2, ESI†) at room temperature, suggesting that the characteristic elongation ratio[25] originating from chain anisotropy[5] was on the order of ~1.9. Note here that in the isotropic case this value is equal to 1.

The cPFOM observations of 25 μm-thick LCEs were performed on the following three situations (Fig. 2). The first one was on the glass-covered LCE surfaces, in which the polydomain formed with the glass covered, using an oil immersion objective lens (with the numerical aperture, NA, of 1.45) (Fig. 2a). The second one was on raw LCE surfaces (Fig. 2b), in which the polydomain formed with nothing (air) on the surface, using a dry objective lens (with the NA of 0.90). The third one was on freeze cracked LCE surfaces using the dry lens (Fig. 2c). The polydomain patterns near the two different, solid or air, boundaries were characterized by the first two observations. The bulk ones were obtained from the third one. The spatial resolutions depended on the lens used, which were characterised separately on the fluorescent nanoparticles embedded within the LCE matrix without the fluorescent probe (Fig. S3, ESI†). The in-plane resolutions were approximately 260 and 330 nm for oiled and dry lenses, respectively. Those in the thickness direction were roughly doubled. These obtained resolutions bound the lower limit of length in texture analysis.

### Polydomain patterns

The typical cPFOM image of our polydomain LCEs is shown in Fig. 2d. Here, we used a coumarin dye (see Experimental) as an anisotropic fluorescent probe that aligns with the local nematic director orientation, **n**, the nematic director vector (note that this is not the refractive index here). Since the probe shows a positive dichroism,[27,28] the brightness of fluorescence directly

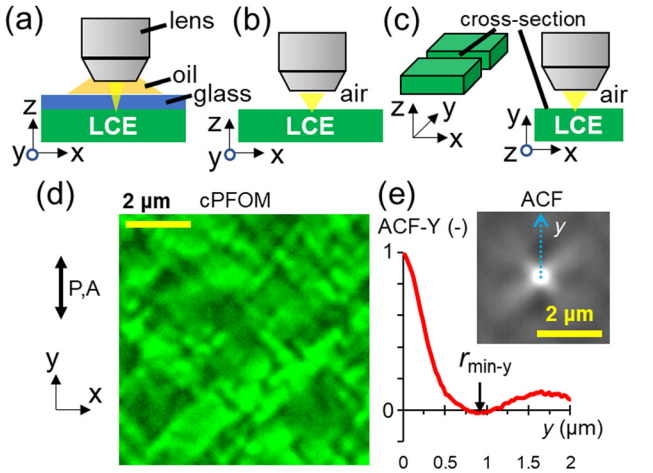


Fig. 2 Three modes of cPFOM observations and a typical image. (a) Glass–LCE interface. (b) Air–LCE interface. (c) Bulk, cross-sectioned surface. (d) Typical polydomain image at air–interface of X3. The bright parts indicate the nematic directors close to the *y* axis. (e) ACF image and the profile in the *y* direction from the center. $r_{min\text{-}y}$ is defined as the first minimum of the ACF in the *y* direction. This value can be used as the index of the correlation length of the nematic ordering in the polydomain texture.

reflects the *y*-component of **n**, the magnitude of **n** projected onto the polariser axis set in the *y*-axis here, indicating that **n** is oriented toward the *y*-axis in bright parts. The roughly rectangular domains with the longer shape in +45° or −45° orientation to the *y* axis appear. Uchida[25] first theoretically predicted using a two-dimensional model that the similar pattern with the ±45° director correlation[35] appeared as a result of the elastic interaction between the neighboring domains, coupled to their nematic order. With this characteristic pattern, the additional strains due to spontaneous elongations in the **n** direction upon development of the nematic order during the polydomain formation are locally accommodated in adjacent domains without macroscopic deformation.

The anisotropic orientational correlation was also seen in the four-leaf pattern of the autocorrelation function image (ACF), $\mathrm{ACF}(\boldsymbol{r}) = \langle n_y(\boldsymbol{r}) n_y(\boldsymbol{r}_0 - \boldsymbol{r}) \rangle_{\boldsymbol{r}_0}$, where $n_y(\boldsymbol{r})$ is the cPFOM intensity, which directly reflects the *y*-component of **n** at the two-dimensional image position $\boldsymbol{r}$ and the sign within brackets indicates the average over the reference point $r_0$ (Fig. 2e). Note that the overall director configuration was macroscopically isotropic confirmed by the similar appearance on sample rotation.[32] Thus, $\mathrm{ACF}(\boldsymbol{r})$ approximately corresponds to the relative orientational correlation function,[25,36] $G_{rel}(\boldsymbol{r})$, of **n** in the polydomain texture. Here, $G_{rel}(\boldsymbol{r}) = \langle \mathrm{ACF}(\boldsymbol{r}) \rangle_{\text{sample-rotation}}$, with the average over rotational angle of the sample while keeping polarizers aligned in the *y* direction. To characterise the average domain length scale, the *y*-profile of the ACF was focused. The length giving the first minimum of the profile was defined as $r_{min\text{-}y}$ and this value was used as an index of the correlation length of interest in the present analysis.

### Effects of boundaries and cross-link densities

The main results are shown in Fig. 3, which highlights the effects of the boundaries and cross-link density on the

polydomain textures. After determining the exact interface point, $d$ = 0, from the cPFOM image stacks at different $z$ positions (Fig. S4, ESI†), the images were analysed regarding ACFs and $r_{min\text{-}y}$. It was defined that $d$ increases as the observation plane moved deeper inside the LCE. Comparing cPFOM images together with their ACFs, the domain size difference was tangible depending on both boundaries and $n_{XD}$. Surprisingly, the domain sizes differed by a factor of 2 to 3 between the glass and the air sides (Fig. 3a–c). The change in $n_{XD}$ of X2, X3, and X10 also drastically alters the indexing domain size, $r_{min\text{-}y}$, from 0.90, 0.63, and 0.48 μm at the bulk.

To further explore the transition of the polydomain structures from the surface to the bulk (Fig. S5–S7, ESI†), $r_{min\text{-}y}$ were plotted with respect to $d$ (Fig. 3d–f). Unfortunately, the reliable

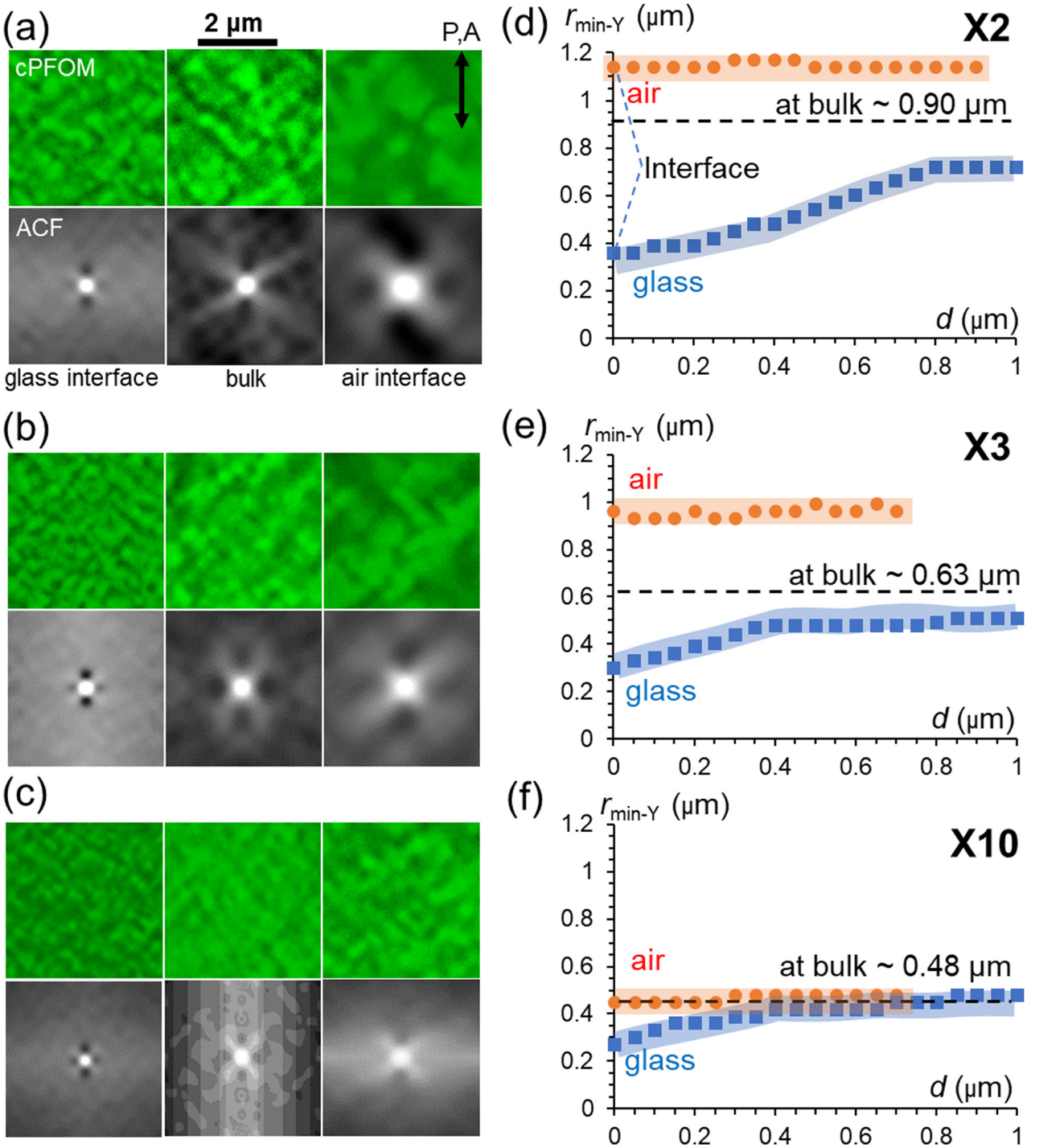


Fig. 3 Polydomain patterns at interfaces and bulk. cPFOM images with the ACFs at glass–LCE ($d_{glass}$ = 0), bulk, and air–LCE interfaces ($d_{air}$ = 0) of (a) X2, (b) X3, and (c) X10. Plots of $r_{min\text{-}y}$ *vs.* $d_{glass/air}$ of (d) X2, (e) X3, and (f) X10.

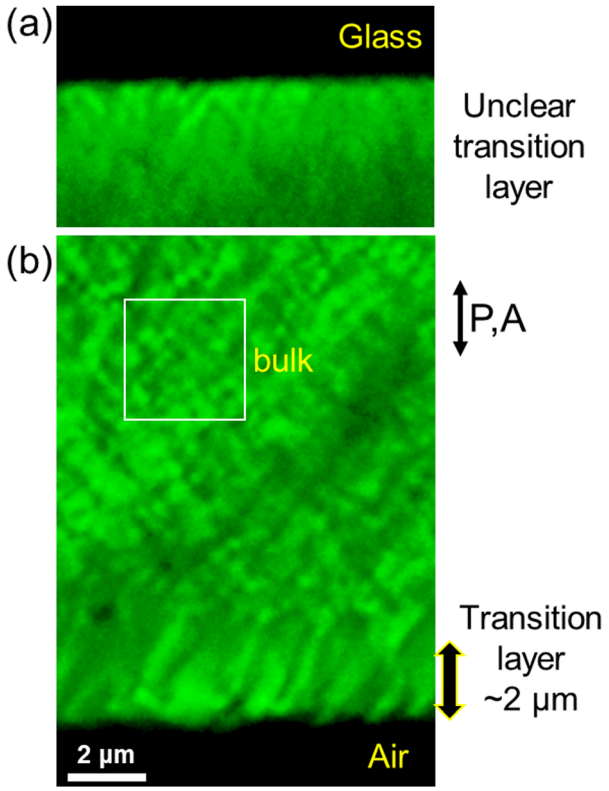


Fig. 4 Cross-sections of X3 close to interfaces. Although the characterization on how polydomain patterns change from the interfaces to the depth was tried on the freeze-cracked cross-sections, the images were rarely obtained. This might be due to the non-flat nature of the cracked surfaces, which made the image evaluation difficult. Nevertheless, those of X3 are shown here. (a) Near the glass–LCE interface the characteristic relative orientational correlation in ±45° directions was observed. However, the transition of polydomain structure was not well resolved. (b) Near the air–LCE interface the transition layer of approximately 2 μm was clearly resolved, in which the long diagonally connected domains appeared. This surface layer differed from that of the bulk polydomain textures at the deeper layer, indicated by a square.

$d$ range was less than 1 μm because of the reduction of the resolution in the depth due to spherical aberration. Nevertheless, at the glass interface side, the trend in which the domain size approached the bulk value is shown. In contrast, at the open interface side, it almost remained constant. In the case of X3, the clear cross-section near the open interface were imaged (Fig. 4) and showed a transition layer of approximately 2 μm with the long diagonally connected domains. The results suggest the longer-ranged boundary effect at the open interface side rather than that at the glass one.

### Theoretical interpretation

The obtained experimental data that first show the clear dependency of the polydomain textures on the two different boundaries and cross-link density are valuable because they are the milestones for controlling them. To assess the physical backgrounds of the observed unique interface- and $n_{XD}$-dependent modifications on the polydomain length scale, we theoretically consider the competition between the nematic ordering and the frozen disorder at the boundary and the bulk.

In the previous work[25] on polydomain nematic LCEs, the frozen disorder is attributed to the random stress introduced upon crosslinking. The average shear strain $\beta$ and the correlation length $l$ of the random stress characterize the frozen disorder. These two parameters are determined by the degree of local nematic order (*i.e.* scalar order parameter) and the orientational correlation size upon crosslinking, respectively. The effective disorder strength in a bulk system is determined by the balance between the random stress and Frank elasticity, and is defined as

$$D = \frac{\mu\alpha\beta l^2}{K},$$

where $\mu$ is the shear modulus of the elastomer in the isotropic phase, $\alpha$ is the degree of anisotropy of the LC polymer in the nematic phase, and $K$ is the Frank elastic constant. Note that the shear modulus $\mu$ is proportional to the crosslink density according to the classical theory of rubber elasticity. According to the numerical simulations for a two-dimensional system,[25] the equilibrium correlation length, *i.e.*, the domain length or size, $r_{min\text{-}y}$, depends on both $D$ and the combination $\mu\alpha^2$, which scales the change of the rubber-elastic energy by the isotropic-nematic transition. The correlation length ($r_{min\text{-}y}$) decreases roughly exponentially as a function of the effective disorder strength $D$. On the other hand, the correlation length increases with $\mu\alpha^2$ for a fixed value of $D$, but this dependence is weaker than the dependence on $D$. Combining these opposing effects, we can predict that the correlation length ($r_{min\text{-}y}$) decreases if only $n_{XD}$ (or $\mu$) is increased. This explains the experimentally observed tendency of the correlation length $r_{min\text{-}y}$ in the bulk samples as $n_{XD}$ is increased from X2 to X3 and then to X10. Furthermore, the ratio between the correlation lengths for X2 and X3 are larger than the ratio between X3 and X10. This might be explained by the observation that the equilibrium correlation size cannot be smaller than that of the frozen disorder.[25] As the correlation size decreases and approaches the disorder correlation length $l$, it shows a weaker dependence on the crosslinking density, as we find in the change from X3 to X10.

On the other hand, the dependence of the correlation length $r_{min\text{-}y}$ on the boundary conditions are presumably originated from the random stress through the effective disorder strength $D$, because $n_{XD}$ and scalar order parameter (reflected in $\mu\alpha^2$) do not differ by the boundary conditions. Note that the random stress produces a long-range deformation and thus remotely affects the director orientation. At the air interface, the random stress is produced only in the half space below surface, and therefore the effective disorder strength $D$ is smaller than in a bulk sample. This would give a reasonable explanation for the larger value of $r_{min\text{-}y}$ for the air interface samples. In contrast, friction at the glass interface will oppose coarsening of the initially microscopic texture. In that sense, it has a similar effect to decreasing the Frank constant $K$ and thus increases the effective disorder strength. However, friction acts only at the

glass interface, and $D$ will recover its bulk value with the depth, which is consistent with the observed behaviour of $r_{\text{min-}y}$. This is different from the air interface case, where the absence of the randomizing sources in the half space has a far-reaching effect and keeps the correlation length almost constant over the depth that is comparable to the bulk correlation length.

## Conclusions

Here, we have shown the tangible effects of the interfaces and cross-link density on the polydomain structures of LCEs. It is also demonstrated that the more precise nature of polydomain textures modulated by interfaces must be carefully considered to yield its accurate measurements, especially on a few micron-thick films. The revealed results are impossible to obtain *via* other conventional observation methods, such as polarised optical microscopy and DPLS. The present results also narrow the range of plausible physical pictures of the polydomain formation and the effects of the interfaces on them. Moreover, the results could be interpreted as follows, in line with the previously reported theoretical model.[25] The dependence of the correlation length on the crosslinking density is qualitatively understood by the combined effect of the effective disorder strength and rubber-elastic energy, which have the opposing effect on the correlation length. On the other hand, the dependence on the boundary conditions is interpreted by the effective disorder strength, which is decreased at the air interface due to the absence of random stress in the air, and is increased by friction at the glass interface. Based on the present knowledge using the cPFOM measurement, the polydomain textures and stripe domains in the more general LCEs can be explored in detail, leading to the development of new optical and/or mechanical functions.

## Experimental

### Materials and preparation of LCE

For preparation of nematic LCE, we modified the methods reported previously,[37–40] and two-step crosslinking reactions, a thiol-acrylate Michael addition and a photoinduced radical polymerization of acrylates were used. The diacrylate monomer, 2-methyl-1,4-phenylene bis(4-(3-(acryloyloxy)propoxy)benzoate) (RM257), was purchased from Wilshire Technologies. Two thiol monomers: 2,2′-(ethylenedioxy)diethanethiol (EDDET) and pentaerythritol tetrakis (3-mercaptopropionate) (PETMP), were purchased from Sigma Aldrich. For the thiol–ene reaction triethylamine (TEA, Sigma Aldrich) was used as the catalyst. Butylated hydroxytoluene (BHT, from Sigma Aldrich) was used as the radical scavenger to suppress the unwanted radical polymerisation reaction between acrylates. Irgacure2959 (Sigma Aldrich) was used as the photoinitiator for LCE with excess acrylates. As the dichroic fluorescent probe, coumarin 545T (C5T, Tokyo Chemical Industry)[28,41] was used. All chemicals were used in their as-received conditions with no purification.

At the specific molar ratio of functional groups shown in Fig. 1b, RM257, EDDET and PETMP were weighed, C5T (0.005 wt%), BHT (0.5 wt%) and Irgacure2959 were added. To parameterize effective cross-link density, the ratios of EDDET and PETMP were varied. After each mixture was gently mixed at an elevated $T \sim 80$ °C for $\sim 10$ min, TEA was added at 1.5–3 wt% to start the first cross-linking reaction between thiol and acrylate groups. The mixture was kept between a glass slide and a cover glass (Cover Glass No. 1 S, Matsunami Glass Ind., Japan) with the spacer with 0.025 mm at 90 °C (isotropic phase) overnight. One side of the sample was released from the glass slide and placed in a vacuum oven at 90 °C overnight for further annealing at the isotropic phase. Note that the solvent had usually been used in the present LCEs,[37–40] but here it was not used to minimize the volumetric change, which might induce unexpected constraint especially in samples with the cover glass. To form the polydomain patterns the samples were quenched to the nematic phase by natural cooling at room temperature. The samples were left for 10 minutes at room temperature and they were then photopolymerised by irradiating ultraviolet (UV) light (365 nm, 200 mm from the lamp source, 8 W, LSUV-8, Az-one) from both sides for 20 min to fix the polydomain patterns. It was confirmed that the polydomain patterns showed no change even after UV irradiation. Some samples after second cross-linking were freeze-cracked in liquid nitrogen, which was far below $T_g$ ($\sim -10$ °C), to observe the cross sections as the bulk polydomain patterns. The reconstruction of the polydomain structures should be avoided even after going back to the room temperature (nematic) from the glass state, because they have been fixed by the secondary cross-linking.

### Three-dimensional (3D) PFOM by confocal laser scanning microscopy

A confocal laser scanning fluorescence microscope ($A1^+$ system, Nikon) was used to characterise polydomain textures at 25 °C (nematic) with the 3D optical resolutions. An optically pumped semiconductor laser (LU-N4 Laser Unit, Nikon, equipped with Sapphire 488, Coherent Inc.) was used to excite the fluorescent probes at 488 nm and the emitted light between 525 and 595 nm was collected. Objective lens with an NA of 1.45 (Plan APO λD 100×, oil, Nikon) or 0.90 (TU Plan Fluor 100×, Nikon) was used for the sample with a cover glass or without it, respectively. The voxel size was of typically $30(x) \times 30(y) \times 50(z)$ nm$^3$. The excitation laser was linearly polarized, and emitted fluorescence in the same polarization was collected using a polariser. On cPFOM images, the brighter parts indicate that the absorption and fluorescence transition dipole moment vectors of the probe have the more components in the polariser direction. Since the present dye molecules align parallelly to the nematic directors of the LCE,[29] the domains observed on the cPFOM images directly reflect the polydomain structure in two-dimension. Given the polarisers along the $y$ axis, the fluorescence intensity reflects the $y$ component $n_y$ of the director $n$. The images were properly deconvoluted using the associated software. The cPFOM images were analysed with respect to the

 

auto-correlation functions (ACFs), which approximately corresponded to the nematic orientational correlation function,[32] and thus, to the average shape of nematic domains in the analysed polydomain texture.

To investigate the effective resolution on the present experimental setup, standard fluorescent beads with the diameter of 100 nm in the present liquid crystal medium were also observed. A LCE sample containing green-fluorescent standard beads with the diameter of 100 nm (FluoSpheres™ F8803, Thermofisher) instead of the C545T dye was observed with the cPFOM with or without the cover glass to gain the aberration effect.

#### Differential scanning calorimetry (DSC)

For differential scanning calorimetry (DSC, DSC4000 PerkinElmer or DSC6100 SII Nanotechnology), samples with approximately 15 mg were loaded into standard aluminium DSC pans. The samples were heated to 100 °C at 10 °C $min^{-1}$, held isothermally for 5 min, and cooled to −50 °C followed by heating up to 100 °C at 5 °C $min^{-1}$ to acquire the data. Although the nematic–isotropic transition peak can be ideally found as the endothermic peak, LCEs with the unclear peak were also checked regarding the clearing temperature by optical observation. The glass transition temperature, $T_g$, was identified as that with the baseline shift at lower $T$ range.

## Author contributions

T. O. conceived the central theme idea. T. O. designed LCEs. T. O. performed the main experiments. K. K. and T. O. performed observations using cPFOM. N. U. led the theoretical interpretation. The results were analysed by T. O., K. K. and N. U. T. O. and N. U. wrote the manuscript, and all authors discussed the results and the manuscript.

## Data availability

The data supporting this article have been included as part of the ESI.† Other data that support the findings of this study are available from the corresponding author upon reasonable request.

## Conflicts of interest

There are no conflicts to declare.

## Acknowledgements

This work was partly supported by Japan Agency for Medical Research and Development (AMED; JP20he0622012) and the Ministry of Education, Culture, Sports, Science and Technology (MEXT) KAKENHI (JP17H06413 and JP17H06417) (K. K.). The authors are grateful for many useful communications from E. M. Terentjev, M. O. Saed, E. Koyama, Y. Norikane, K. Saitoh, and Y. Kikkawa.

## Notes and references

1 P. G. de Gennes and J. Prost, *The Physics of Liquid Crystals*, Oxford University Press, New York, 2nd edn, 1993.
2 D. C. Prevorsek, in *Polymer Liquid Crystals*, ed. A. Ciferri, W. R. Krigbaum and R. B. Meyer, Academic Press, New York, 1982, pp. 329–376.
3 D. W. Berreman, *Phys. Rev. Lett.*, 1972, **28**, 1683–1686.
4 J. I. Fukuda, M. Yoneya and H. Yokoyama, *Phys. Rev. Lett.*, 2007, **98**, 1–4.
5 M. Warner and E. M. Terentjev, *Liquid Crystal Elastomers*, Oxford Univ. Press, New York, 2007.
6 J. Küpfer and H. Finkelmann, *Makromol. Chem., Rapid Commun.*, 1991, **12**, 717–726.
7 P.-G. De Gennes, M. Hébert and R. Kant, *Macromol. Symp.*, 1997, **113**, 39–49.
8 F. Elias, S. M. Clarke, R. Peck and E. M. Terentjev, *Europhys. Lett.*, 1999, **47**, 442–448.
9 T. Ohzono and E. Koyama, *Macromol. Rapid Commun.*, 2024, **2300709**, 1–10.
10 T. Ohzono and E. Koyama, *Macromolecules*, 2023, **56**, 5346–5355.
11 M. Warner, P. Bladon and E. M. Terentjev, *J. Phys. II*, 1994, **4**, 93–102.
12 A. DeSimone and G. Dolzmann, *Arch. Ration. Mech. Anal.*, 2002, **161**, 181–204.
13 I. Kundler and H. Finkelmann, *Macromol. Rapid Commun.*, 1995, **16**, 679–686.
14 H. Finkelmann, I. Kundler, E. M. Terentjev and M. Warner, *J. Phys. II*, 1997, **7**, 1059–1069.
15 G. C. Verwey, M. Warner and E. M. Terentjev, *J. Phys. II*, 1996, **6**, 1273–1290.
16 E. R. Zubarev, S. A. Kuptsov, T. I. Yuranova, R. V. Talroze and H. Finkelmann, *Liq. Cryst.*, 1999, **26**, 1531–1540.
17 Y. Zhang, Z. Zhang and Y. Huo, *J. Mech. Phys. Solids*, 2020, **144**, 104110.
18 L. A. Mihai and A. Goriely, *MRS Bull.*, 2021, **46**, 784–794.
19 D. Mistry and H. F. Gleeson, *J. Polym. Sci., Part B: Polym. Phys.*, 2019, **57**, 1367–1377.
20 E. Fried and S. Sellers, *J. Appl. Phys.*, 2006, **100**, 043521.
21 M. De Luca, A. Desimone, A. Petelin and M. Čopič, *J. Mech. Phys. Solids*, 2013, **61**, 2161–2177.
22 T. Ohzono, H. Minamikawa and E. M. Terentjev, *Commun. Mater.*, 2022, **3**, 29.
23 T. Ohzono and E. Koyama, *Macromol. Rapid Commun.*, 2022, **43**, 2200599.
24 S. V. Fridrikh and E. M. Terentjev, *Phys. Rev. E: Stat. Phys., Plasmas, Fluids, Relat. Interdiscip. Top.*, 1999, **60**, 1847–1857.
25 N. Uchida, *Phys. Rev. E:Stat. Phys., Plasmas, Fluids, Relat. Interdiscip. Top.*, 2000, **62**, 5119–5136.
26 N. Uchida and A. Onuki, *Europhys. Lett.*, 1999, **45**, 341–347.
27 T. Ohzono, K. Katoh, C. Wang, A. Fukazawa, S. Yamaguchi and J. I. Fukuda, *Sci. Rep.*, 2017, **7**, 1–13.
28 T. Ohzono, T. Yatabe, C. Wang, A. Fukazawa and S. Yamaguchi, *Commun. Chem.*, 2018, **1**, 52.

29 T. Ohzono, K. Katoh, H. Minamikawa, M. O. Saed and E. M. Terentjev, *Nat. Commun.*, 2021, **12**, 787.
30 I. I. Smalyukh and O. D. Lavrentovich, *Phys. Rev. E:Stat., Nonlinear, Soft Matter Phys.*, 2002, **66**, 16.
31 S. M. Clarke, E. Nishikawa, H. Finkelmann and E. M. Terentjev, *Macromol. Chem. Phys.*, 1997, **198**, 3485–3498.
32 T. Ohzono, K. Katoh and E. M. Terentjev, *Macromolecules*, 2021, **54**, 3678–3688.
33 J. Nehring and A. Saupe, *J. Chem. Soc., Faraday Trans. 2*, 1972, **68**, 1–15.
34 C. Chiccoli, I. Feruli, O. D. Lavrentovich, P. Pasini, S. V. Shiyanovskii and C. Zannoni, *Phys. Rev. E: Stat., Nonlinear, Soft Matter Phys.*, 2002, **66**, 1–4.
35 A. Duzgun and J. V. Selinger, *Phys. Rev. Lett.*, 2015, **115**, 1–5.
36 N. Uchida and T. Ohzono, *Soft Matter*, 2010, **6**, 5729–5735.
37 D. P. Nair, N. B. Cramer, J. C. Gaipa, M. K. McBride, E. M. Matherly, R. R. McLeod, R. Shandas and C. N. Bowman, *Adv. Funct. Mater.*, 2012, **22**, 1502–1510.
38 C. M. Yakacki, M. Saed, D. P. Nair, T. Gong, S. M. Reed and C. N. Bowman, *RSC Adv.*, 2015, **5**, 18997–19001.
39 M. O. Saed, R. H. Volpe, N. A. Traugutt, R. Visvanathan, N. A. Clark and C. M. Yakacki, *Soft Matter*, 2017, **13**, 7537–7547.
40 T. Ohzono, M. O. Saed and E. M. Terentjev, *Adv. Mater.*, 2019, **31**, 1902642.
41 C. H. Chen and C. W. Tang, *Appl. Phys. Lett.*, 2001, **79**, 3711–3713.